



UNIVERSITY OF LEEDS

This is a repository copy of *Uncertainty quantification of wall shear stress in intracranial aneurysms using a data-driven statistical model of systemic blood flow variability*.

White Rose Research Online URL for this paper:
<http://eprints.whiterose.ac.uk/134505/>

Version: Accepted Version

Article:

Sarrami-Foroushani, A, Lassila, T orcid.org/0000-0001-8947-1447, Gooya, A et al. (2 more authors) (2016) Uncertainty quantification of wall shear stress in intracranial aneurysms using a data-driven statistical model of systemic blood flow variability. *Journal of Biomechanics*, 49 (16). pp. 3815-3823. ISSN 0021-9290

<https://doi.org/10.1016/j.jbiomech.2016.10.005>

© 2016 Elsevier Ltd. All rights reserved. Licensed under the Creative Commons Attribution-Non Commercial No Derivatives 4.0 International License (<https://creativecommons.org/licenses/by-nc-nd/4.0/>).

Reuse

This article is distributed under the terms of the Creative Commons Attribution-NonCommercial-NoDerivs (CC BY-NC-ND) licence. This licence only allows you to download this work and share it with others as long as you credit the authors, but you can't change the article in any way or use it commercially. More information and the full terms of the licence here: <https://creativecommons.org/licenses/>

Takedown

If you consider content in White Rose Research Online to be in breach of UK law, please notify us by emailing eprints@whiterose.ac.uk including the URL of the record and the reason for the withdrawal request.



eprints@whiterose.ac.uk
<https://eprints.whiterose.ac.uk/>

Uncertainty quantification of wall shear stress in intracranial aneurysms using a data-driven statistical model of systemic blood flow variability

Ali Sarrami-Foroushani^a, Toni Lassila^a, Ali Gooya^a, Arjan J. Geers^b,
Alejandro F. Frangi^{a,*}

^a*Centre for Computational Imaging and Simulation Technologies in Biomedicine (CISTIB),
Department of Electronic and Electrical Engineering, The University of Sheffield, Sheffield,
UK*

^b*Centre for Cardiovascular Science, University of Edinburgh, UK*

Abstract

Adverse wall shear stress (WSS) patterns are known to play a key role in the localisation, formation, and progression of intracranial aneurysms (IAs). Complex region-specific and time-varying aneurysmal WSS patterns depend both on vascular morphology as well as on variable systemic flow conditions. Computational fluid dynamics (CFD) has been proposed for characterising WSS patterns in IAs; however, CFD simulations often rely on deterministic boundary conditions that are not representative of the actual variations in blood flow. We develop a data-driven statistical model of internal carotid artery (ICA) flow, which is used to generate a virtual population of waveforms used as inlet boundary conditions in CFD simulations. This allows the statistics of the resulting aneurysmal WSS distributions to be computed. It is observed that ICA waveform variations have limited influence on the time-averaged WSS (TAWSS) on the IA surface. In contrast, in regions where the flow is locally highly multidirectional, WSS directionality and harmonic content are strongly affected by the ICA flow waveform. As a consequence, we argue that the effect of blood flow variability should be explicitly considered in CFD-based IA rupture assessment

[☆] Author Postprint Version - Journal of Biomechanics - October 11, 2016

*Corresponding author: Alejandro F. Frangi, e-mail: a.frangi@sheffield.ac.uk,
tel: +44 114 2220153, fax: +44 114 2227890

to prevent confounding the conclusions.

Keywords: intracranial aneurysms, multidirectional flow, wall shear stress, computational fluid dynamics, uncertainty quantification

1 **Introduction**

2 Pro-inflammatory responses in the vascular endothelium play a key role in
3 intracranial aneurysm (IA) growth and rupture (Meng et al., 2014). The driv-
4 ing factor behind this response is hypothesised to be wall shear stress (WSS),
5 defined as the frictional force of blood on the vessel wall. Localised adverse
6 WSS patterns, i.e., spatiotemporal distribution of hemodynamic WSS on the
7 aneurysm sac, have been shown by Feaver et al. (2013) to correlate with the ex-
8 pression of transcription factors related to inflammation (such as NF- κ B), and
9 have been shown by Davies (2009), Chiu and Chien (2011) and, Mohamied et al.
10 (2015) to correlate with locations of atherosclerotic lesions on the vessel wall.
11 Several attempts have been made to further characterise the atherogenic WSS
12 patterns by looking into, e.g., WSS magnitude oscillations (Lee et al., 2009; Ku
13 et al., 1985), temporal and spatial gradients (DePaola et al., 1992; Dolan et al.,
14 2013), and the harmonic content of the WSS waveforms (Feaver et al., 2013;
15 Himburg and Friedman, 2006).

16 Evaluation of WSS from phase contrast magnetic resonance imaging is not
17 reliable enough to provide quantitative measures (Boussel et al., 2009). There-
18 fore, computational fluid dynamics (CFD) has been proposed as a tool for char-
19 acterising WSS patterns. WSS multidirectionality has been recently used to
20 characterise atherogenic flows in CFD simulation studies by Mohamied et al.
21 (2015), and Peiffer et al. (2013a). However, CFD-based studies are contro-
22 versial among interventional neuroradiologists and have not become widely ac-
23 cepted in clinical decision making. Such controversies can be found in e.g.
24 Kallmes (2012), Cebal and Meng (2012), Valen-Sendstad and Steinman (2014),
25 and Xiang et al. (2014b), where the clinicians and CFD modellers discussed
26 the confounding nature and unreliability of various CFD-based haemodynamic

27 variables and the importance of assumptions and uncertainties associated to
28 CFD models. Failure to address underlying variations in systemic blood flow
29 due to the state of the patient (e.g., level of stress, physical activity, sleep, etc.)
30 and its effect on WSS patterns may be one of the reasons behind this perceived
31 unreliability.

32 Our primary aim is to quantify the effect of flow waveform variability on the
33 hemodynamic WSS over the intracranial aneurysm surface. Boundary condi-
34 tions in CFD models are typically either drawn from literature data or obtained
35 by patient-specific flow imaging over a few heartbeats. Neither approach re-
36 produces the *intra-subject variability* of systemic blood flow arising due to the
37 presence of dynamic regulatory systems. The sensitivity of the intra-aneurysmal
38 haemodynamics to the systemic flow conditions has been explored in various
39 studies. For example, Geers et al. (2014) found a 20% increase in flow rate to
40 correspond to a 27% increase in aneurysmal WSS; Xiang et al. (2014a) found
41 different flow rate waveforms with the same time-averaged inflow rate to produce
42 almost identical WSS distributions and WSS magnitudes, similar OSI distribu-
43 tions, but drastically different OSI values; and Morales and Bonnefous (2015)
44 observed that the spatiotemporal-averaged aneurysmal WSS varies quadrati-
45 cally with the inflow rate. However, CFD models of vascular blood flow still
46 mostly report deterministic flow results.

47 To address this problem, we construct a Gaussian process model (GPM) for
48 generating internal carotid artery (ICA) waveforms. The GPM is calibrated
49 against the data from Ford et al. (2005) on ICA flow measurements across a
50 cohort of 17 young adults. The variability due to flow uncertainty is measured
51 in three quantities of interest: time averaged WSS (TAWSS), oscillatory shear
52 index (OSI), and transverse WSS (TransWSS), and means and confidence in-
53 tervals are computed for each. In this way, we achieve a novel combination of
54 CFD simulations and statistical models that: 1) incorporates physiological flow
55 measurements, 2) is more systematic than previous approaches for quantifying
56 flow uncertainty, and 3) can be fitted to the characteristics of particular cohorts.

57 Classifying IAs by their rupture likelihood is currently performed by look-

58 ing at morphological features and patient-specific risk factors (Bederson et al.,
59 2000). Machine learning has been proposed to aid in this task. Xiang et al.
60 (2011) used morphological and hemodynamic features assessed on a cohort of
61 119 patients to train a logistic regression model for IA classification. Bisbal et al.
62 (2011) performed an exhaustive evaluation of seven different classifiers trained
63 on 60 different features identified as being significant. Using the bounds on
64 WSS uncertainty computed in this study, we explore what happens when flow
65 uncertainties are incorporated into a classifier similar to that of Xiang et al.
66 (2011). The results demonstrate that the effect of flow variability on IA classi-
67 fiers should be explicitly considered to avoid biasing effects that may confound
68 the conclusions of CFD studies used to predict IA rupture likelihood.

69 **Materials and Methods**

70 *Image-based patient-specific intracranial aneurysm models*

71 Patient-specific surface models for two saccular IAs from the @neurIST co-
72 hort were previously reconstructed from three-dimensional rotational angiogra-
73 phy as described in by Villa-Uriol et al. (2011) using the geodesic active regions
74 approach of Bogunović et al. (2011). Both IAs were located on the ophthalmic
75 segment of the left internal carotid artery. During the follow-up period, the
76 aneurysm in patient 1 ruptured, whereas the one in patient 2 did not rupture.
77 Vascular models were discretised using unstructured volumetric meshes in AN-
78 SYS ICEM v16.2 (Ansys Inc., Canonsburg, PA, USA). Tetrahedral elements
79 with maximum edge size of 0.2 mm were used and three layers of prismatic
80 elements with an edge size of 0.1 mm were used to create boundary layers. The
81 total number of elements were 2.2 and 6.6 million and mesh densities were 3025
82 and 3315 elements per mm^3 for patients I and II, respectively.

83 *Computational fluid dynamics simulations*

84 Blood flow in the IA was modelled using the incompressible unsteady Navier-
85 Stokes equations. Blood was assumed to be a Newtonian fluid of density 1066

86 kg/m³ and viscosity of 0.0035 Pa·s. Peak systolic Reynolds numbers at the
87 inlet ranges from 338 to 532, and no turbulence modelling was performed. To
88 ensure fully-developed flow, the computational domain was extended at the inlet
89 boundary by an entrance length proportional to the inlet boundary maximum
90 Reynolds number. The Navier-Stokes equations were solved in ANSYS CFX
91 v16.2 (Ansys Inc., Canonsburg, PA, USA) using a finite-volume method. The
92 cardiac cycle was discretised in time into 200 equal steps. Element and time-
93 step sizes were set according to the @neurIST processing toolchain where mesh
94 and time-step size independency tests were performed on WSS, pressure, and
95 flow velocity at several points in the computational domain as described by
96 Villa-Uriol et al. (2011). Arterial distensibility was not considered in this study
97 (rigid-wall assumption).

98 *Inlet boundary conditions and generation of ICA waveforms*

99 A Gaussian process model (GPM) (see e.g. Williams and Rasmussen (2006)
100 for details) was used to generate multiple inflow waveforms that mimicked the
101 inter-subject flow variability at the ICA. The GPM was trained on subject-
102 specific data from the study of Ford et al. (2005) describing ICA flow measure-
103 ments in 17 young adults. In that work, descriptive statistics of the reference
104 flow rate waveform were reported in terms of mean values and variances of both
105 time and flow rate at 14 fiducial landmarks. Flow rate mean values and vari-
106 ances were used to generate the GPM in this study. Any GPM is defined by its
107 mean waveform plus a covariance function. Since the ICA flow waveform was
108 smooth, continuous, and differentiable, the covariance function was chosen to be
109 a squared exponential, $\sigma^2(t_j, t_k) = \sigma_0^2 \exp(-\|t_j - t_k\|_T^2 / 2L^2)$, with parameters
110 σ_0 and L (Williams and Rasmussen, 2006). The distance metric was chosen
111 as $\|t_j - t_k\|_T := \min\{|t_j - t_k|, |t_j - t_k + T_{\text{period}}|, |t_j - t_k - T_{\text{period}}|\}$ to get pe-
112 riodic waveforms, where T_{period} was the normalised cardiac cycle length and
113 $t_j, t_k \in [0, T]$. As a stationary Gaussian process could not fully fit the observed
114 data (variance at systolic peak was greater than during diastole), a symmetric
115 bell-shaped function, f , was used to introduce non-stationarity in the process.

$$f(t_j, t_k) = s_d + \frac{1}{\frac{1}{s_{ps}} + \left| \frac{\max(t_j, t_k) - x_{ps}}{2} \right|^4} \quad (1)$$

116 In equation (1), $s_d \in [0, 1]$ and $s_{ps} \in [0, 1]$ are parameters controlling the
 117 variance during diastole and at peak systole, respectively; and, x_{ps} is the peak
 118 systolic landmark number. As reported by Ford et al. (2005), the ICA waveform
 119 systolic variance is approximately four times greater than diastolic variance and
 120 the systolic peak is the third landmark on the ICA waveform. Thus, in equation
 121 (1) the parameter s_{ps} was replaced by $4s_d$ and x_{ps} was set to 3.

122 Finally, the GPM mean waveform was set to the mean ICA waveform taken
 123 from Ford et al. (2005); and the GPM covariance function $\sigma^2(t_j, t_k)$ was con-
 124 structed as

$$\sigma^2(t_j, t_k) = f(t_j, t_k) \cdot \sigma_0^2 \cdot \exp\left(-\min\{|t_j - t_k|, |t_j - t_k + T_{\text{period}}|, |t_j - t_k - T_{\text{period}}|\} / 2L^2\right). \quad (2)$$

125 Random realisations of the GPM was then used GPM-generated ICA wave-
 126 forms. To fit the process covariance σ_0^2 and correlation length L to that observed
 127 in the measurements, for each $s_d \in [0, 1]$, a two-dimensional numerical optimi-
 128 sation problem was solved based on the cost function, g , that penalised values
 129 exactly equal to the mean waveform or greater than twice the standard deviation
 130 for each landmark.

$$g(y_j) = \begin{cases} P_o(y_j - (\bar{y}_j + 2SD_j)) & \bar{y}_j + 2SD_j \leq y_j \\ \frac{-P_m}{2SD_j}|y_j - \bar{y}_j| + P_m & \bar{y}_j - 2SD_j \leq y_j \leq \bar{y}_j + 2SD_j \\ P_o(y_j - (\bar{y}_j - 2SD_j)) & y_j \leq \bar{y}_j - 2SD_j \end{cases} \quad (3)$$

131 For each landmark j , y_j is the value of ICA flow generated by the GPM;
 132 and, \bar{y}_j and SD_j are the mean and standard deviation reported by Ford et al.
 133 (2005). Penalty parameters P_m and P_o penalise y_i values that are exactly equal
 134 to the mean or are deviated more than twice the standard deviation from the
 135 mean.

136 A virtual population of 50 internal carotid flow waveforms was then gener-
137 ated and used as inlet boundary conditions to the CFD models. To maintain
138 a physiological arterial WSS of 1.5 Pa and to enable population-wide compar-
139 isons, Poiseuille’s law was used to scale the GPM-generated waveforms such
140 that the time-averaged WSS was 1.5 Pa at the inlet. Fig. 1(a) shows the 95%
141 confidence bounds of flow at the fiducial landmarks (black bars), and a virtual
142 population of internal carotid artery flow waveforms generated from the Gaus-
143 sian process model (red curves). More details about GP modelling of the ICA
144 flow waveforms are presented in the Supplementary Material.

145 *Outlet boundary conditions*

146 A two-element windkessel (RC) boundary condition model was assigned at
147 the outlet boundaries. The RC windkessel model acts as a low-pass filter with
148 a RC time constant $\tau = R \times C$. To guarantee that the terminal RC circuit
149 converges to the ultimate pulsatile pressure and the solution is independent
150 from the initial transient numerical effects, each simulation was run for certain
151 number of cycles, defined as $nCycle = \left\lceil \frac{\tau}{T_{period}} \right\rceil + 1$, where $\lceil x \rceil$ symbolized the
152 ceil function. Results from the last cardiac cycle were then used to calculate
153 the hemodynamic parameters of interest. The resistance and capacitance values
154 of the windkessel model were chosen to maintain a physiological range of ICA
155 pressure and pulsatility for each particular patient. To enable rapid parameter
156 tuning, a surrogate model was built using polynomial response surfaces to ap-
157 proximate the mean arterial pressure (MAP) and pressure wave pulsatility index
158 (PPI) of the flow for each (R,C) pair. A Chebyshev grid of 81 (9×9) points was
159 created on a 2D physiological range of variability for R and C (reported in e.g.
160 Brown et al. (2012); Reymond et al. (2011, 2009); Stergiopoulos et al. (1992);
161 Vignon-Clementel et al. (2010)) in such a way that each point on the grid was
162 associated with a pair of R and C values. A total of 81 CFD simulations were
163 performed while recording the observed values of steady-state mean arterial
164 pressure (MAP) and pressure wave pulsatility index (PPI) in the ICA for each
165 simulation after $nCycle$ heartbeat cycles. To develop a surrogate model of ICA

166 MAP and PPI vs terminal resistance and capacitance, MAP and PPI surfaces
 167 were linearly interpolated over a uniform grid of 100×100 . The surrogate model
 168 was used to select values R and C values in such a way that when the reference
 169 inflow waveform were applied at the inlet boundary, the model provides ICA
 170 pressures with MAP and PPI matching clinically measured values of 90 mmHg
 171 and 0.5 from the normal individual, respectively. Fig. 1(b) and Fig. 1(c). show
 172 the response surfaces of MAP and PPI against terminal resistance and capac-
 173 itance for patient 1. Fig. 1(d), values of R and C at the point, where MAP
 174 = 90 mmHg and PPI = 0.5 intersects, were selected as optimized windkessel
 175 parameters for patient 1. As mentioned above, a derivation of the Poiseuille's
 176 law that relates the inflow rate to the WSS and vessel's inlet cross-sectional
 177 area was used to scale the time-averaged flow rate in the parent vessel for each
 178 patient. Since the time-averaged flow rates are different in patient 2, the re-
 179 sistance and capacitance values from the first patient's surrogate model need
 180 to be scaled using factor α defined as $\alpha = \text{inflow}_{tav,1} / \text{inflow}_{tav,2}$, where
 181 $\text{inflow}_{tav,1}$ and $\text{inflow}_{tav,2}$ are time-averaged inflow rates for patients 1 and 2.
 182 The terminal resistance and capacitance were then scaled as $R_2 = (1/\alpha) \times R_1$
 183 and $C_2 = \alpha \times C_1$, respectively.

184 Fig. 1(e) shows reference inflow waves for patients 1 and 2. Fig. 1(f) shows
 185 that, applying the windkessel outlet boundary condition with tuned R and C
 186 values, the same desired ICA pressure has been obtained for patients 1 and 2
 187 with different inflow waveforms. Since the time-averaged inflow rate was kept
 188 constant and only waveform shapes varied across the virtual population, the
 189 same R and C values as those tuned with the reference inflow waveforms were
 190 used for all 50 CFD simulations on each patient.

191 *Data analysis*

192 Wall shear stress (WSS), $\tau_w(x, t)$, is a time-varying vector field that repre-
 193 sents the tangential component of the traction vector on the wall. We assessed
 194 the magnitude, pulsatility, directionality and the harmonic content of the WSS
 195 waveforms on the aneurysm wall using several derived quantities of interest.

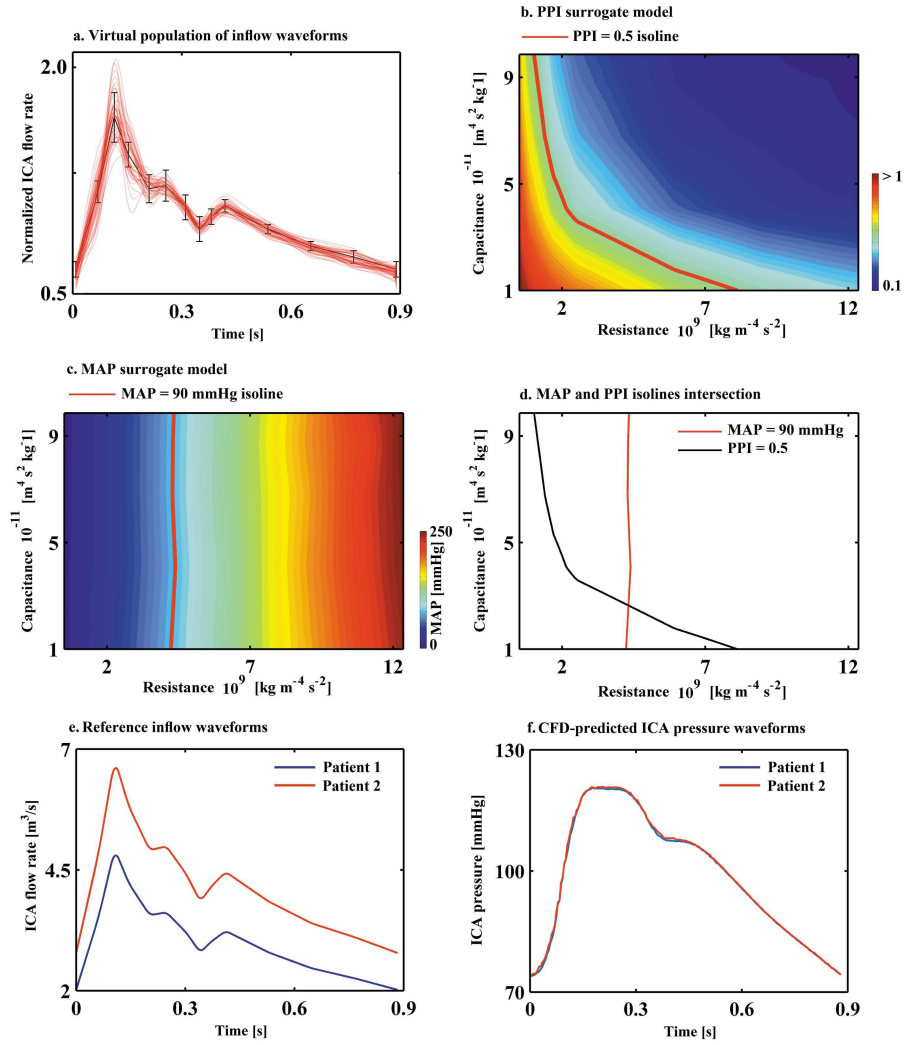


Figure 1: a) Response surface of the surrogate model of the internal carotid (ICA) mean arterial pressure (MAP). ICA MAP is 90 mmHg on the red solid line. b) Response surface surrogate model of the internal carotid (ICA) pressure pulsatility index (PPI). ICA PPI is 0.5 on the red solid line. c) Intersection of the MAP and the PPI isolines gives the right terminal resistance (R) and capacitance (C) values for the desired MAP and PPI at the ICA. d) Reference flow rate waveforms for patients 1 and 2 that are scaled such that the time-averaged wall shear stress (WSS) at the inlet was 1.5 Pa for each patient. e) CFD-predicted pressure waveforms at the ICA after choosing the right R and C values.

196 *WSS magnitude*

197 Time-averaged WSS (TAWSS) was calculated by averaging the magnitude
198 of WSS vector at each surface node over the cardiac cycle.

$$\text{TAWSS}(x) = \frac{1}{T_{\text{period}}} \int_{T_0}^{T_0+T_{\text{period}}} |\boldsymbol{\tau}_w(x, t)| dt \quad (4)$$

199 The variables T_0 and $T_0 + T_{\text{period}}$ are the starting point (3rd heartbeat) and
200 the length of the cardiac cycle over which the WSS was integrated, respectively.

201 *WSS directionality*

202 As suggested by Mohamied et al. (2015) and Peiffer et al. (2013a,b), to assess
203 the directionality of WSS we used both OSI and TransWSS. The oscillatory
204 shear index was calculated as

$$\text{OSI} = \frac{1}{2} \left(1 - \frac{|\int_{T_0}^{T_0+T_{\text{period}}} \boldsymbol{\tau}_w(x, t) dt|}{\int_0^{T_{\text{period}}} |\boldsymbol{\tau}_w(x, t)| dt} \right) \quad (5)$$

205 and transverse WSS was calculated as defined by Peiffer et al. (2013a)

$$\text{transWSS} = \frac{1}{T_{\text{period}}} \int_{T_0}^{T_0+T_{\text{period}}} |\boldsymbol{\tau}_w(x, t) \cdot \hat{q}| dt, \quad (6)$$

206 where $\hat{q} = \hat{p} \times \hat{n}$ and the unit vector \hat{p} is the direction of the time-averaged
207 WSS vector, \hat{n} is the surface normal, and consequently the unit vector \hat{q} is
208 located in the same plane as \hat{p} and its direction is perpendicular to the time-
209 averaged WSS vector. The unit vector \hat{p} was calculated as

$$\hat{p} = \frac{\int_{T_0}^{T_0+T_{\text{period}}} \boldsymbol{\tau}_w(x, t) dt}{|\int_{T_0}^{T_0+T_{\text{period}}} \boldsymbol{\tau}_w(x, t) dt|} \quad (7)$$

210 As long as a preferred time-averaged direction of flow exists, TransWSS
211 ranges from 0 to TAWSS. As the TAWSS takes substantially different values
212 at aneurysmal regions with disturbed or regular flow, we defined the relative
213 transWSS (rTransWSS) as the TransWSS normalised TransWSS by the TAWSS
214 at each surface point.

215 *WSS harmonics*

216 As indicated by Lee et al. (2009), despite the multidirectional nature of
217 blood flow in patient-specific vascular models, most experimental studies are
218 performed under uniaxial flow due to constraints in experimental flow setups.
219 Recently, WSS projections onto a reference axial direction were performed to
220 rectify multidirectional flows and make them comparable to the flows used for *in*
221 *vitro* experiments of Arzani and Shadden (2016) and Morbiducci et al. (2015).
222 However, since rectifying the WSS signal combines the magnitude and direction-
223 ality aspects of the WSS vector and influences its harmonic content, we chose to
224 perform a harmonic analysis on both the original and the rectified WSS signals.
225 It has been observed that most physiological waveforms can be accurately re-
226 constructed by the first ten or fewer harmonics (Nichols et al., 2011). Studying
227 the first eight harmonics of the WSS signals at the ICA, Feaver et al. (2013)
228 showed that the endothelial inflammatory responses are mainly regulated by
229 the first harmonic of the WSS signal. Thus, in this study, we based our har-
230 monic analyses on the first eight harmonics of the WSS signals. We calculated
231 the axial WSS as the component of time-varying WSS vector projected onto
232 the unit vector \hat{p} . The fast Fourier transform was used to describe the time-
233 varying aneurysmal WSS and axial WSS waveforms in the frequency domain
234 and extract the amplitudes of the harmonics zeroth to eighth. It has been hy-
235 pothesised that dominance of frequencies higher than the heart rate in the WSS
236 magnitude signal triggers inflammatory responses in the vascular endothelium
237 (Himburg et al., 2007; Feaver et al., 2013). The dominant harmonic (DH) is
238 another quantity of interest defined as the harmonic with the greatest ampli-
239 tude by Himburg and Friedman (2006). As shown by Lee et al. (2009), DH is
240 independent from other WSS-related variables. In this study we also used DH
241 to investigate how waveform variability in the parent vessel affect the dominant
242 frequency of the time-varying WSS magnitude over the aneurysm sac.

244 To evaluate the effect of WSS uncertainty in IA rupture prediction, a differ-
 245 ent subset of 38 IAs all located at the sylvian bifurcation of the middle cerebral
 246 artery (MbifA-type) were selected from the @neurIST cohort and processed
 247 through the CFD pipeline as described in the Methods section. For this co-
 248 hort, outlet branches were automatically clipped 20 mm after their proximal
 249 bifurcation. Branches shorter than 20 mm were extruded before truncation.
 250 Zero-pressure boundary conditions were then imposed at all outlets. As a full
 251 CFD simulation of all 50×38 cases would have been prohibitively costly, three
 252 representative waveforms were instead used for each of the 38 cases: mean flow,
 253 minimum flow and maximum flow predicted by the GPM model. TAWSS, OSI,
 254 and TransWSS were post-processed for each of these simulations and spatially
 255 averaged over the aneurysm sac to arrive at the feature values used for classifi-
 256 cation. These three different flow waveforms were then used to train a logistic
 257 regression model classifier similar to that of Xiang et al. (2011):

$$\text{logit}(P_r) = \beta_0 + \beta_1 \text{OSI} + \beta_2 \text{TAWSS},$$

258 where P_r is the model-predicted probability that the aneurysm was of the
 259 ruptured type, and the logit function is defined as $\text{logit}(p) = \log\left(\frac{p}{1-p}\right)$. The
 260 regression coefficients $\beta_0, \beta_1, \beta_2$ were obtained through standard generalised
 261 regression techniques, and were used to define the corresponding odds ratios
 262 ($\text{OR}_{\text{OSI}} = \exp(\beta_1)$ etc.), signifying how the odds of rupture increase by each
 263 unit increase in OSI.

264 **Results**

265 Fig. 2 shows the mean values and the coefficients of variation (CoV) for
 266 TAWSS, OSI, and rTransWSS on the aneurysm sac simulated by CFD over the
 267 population of 50 difference ICA waveforms. In both cases, the ICA waveform
 268 variability had limited effects ($\text{CoV} < 0.05$) on the TAWSS. However, the ef-
 269 fects were remarkable on WSS directional variability. CoVs for aneurysmal OSI

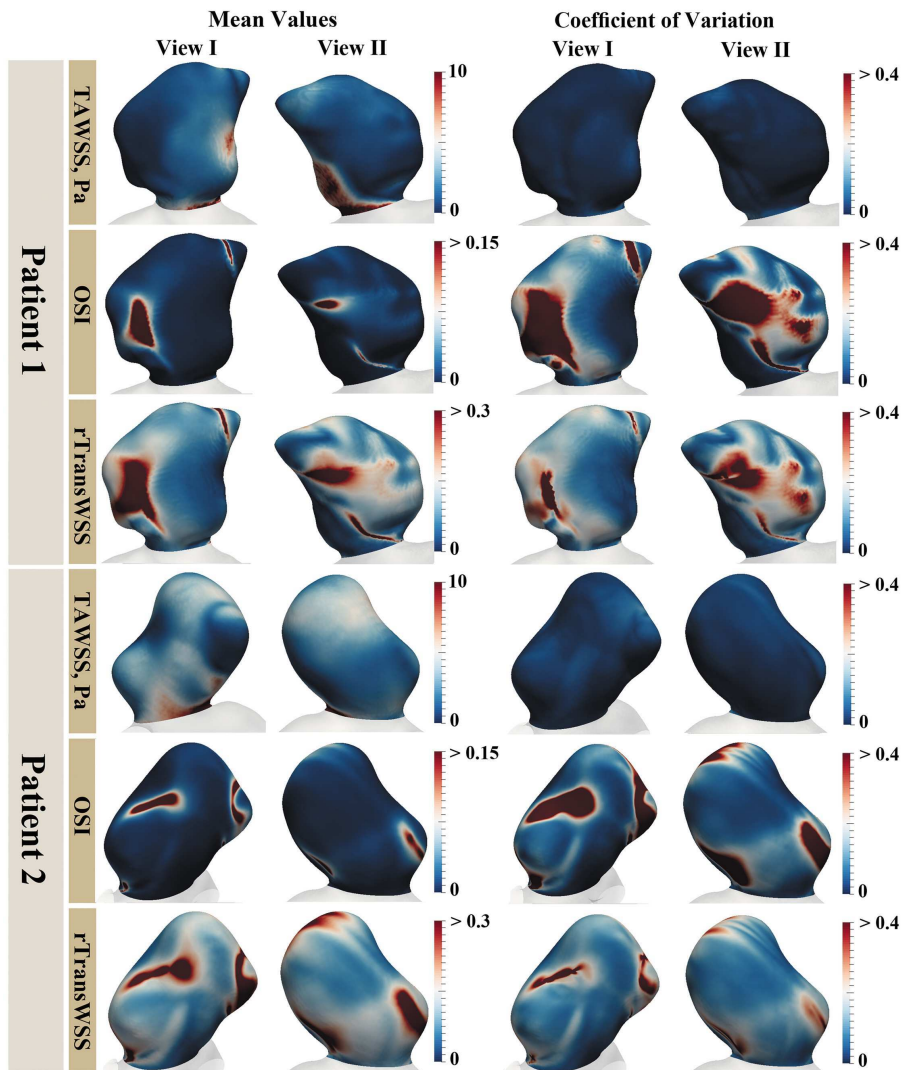


Figure 2: The mean values and the coefficients of variation (CoV) of the time-averaged WSS magnitude (TAWSS), the oscillatory shear index (OSI), and the relative transverse WSS (rTransWSS) across the virtual population over the aneurysm walls for patients 1 and 2.

270 and rTransWSS were both greater than 0.4 at regions where the WSS vectors
 271 had low magnitude but were directionally varying in time (disturbed flow re-
 272 gions). Waveform variability in the parent vessel had less significant effects on
 273 the WSS directionality at regions where shear stresses are higher and remain

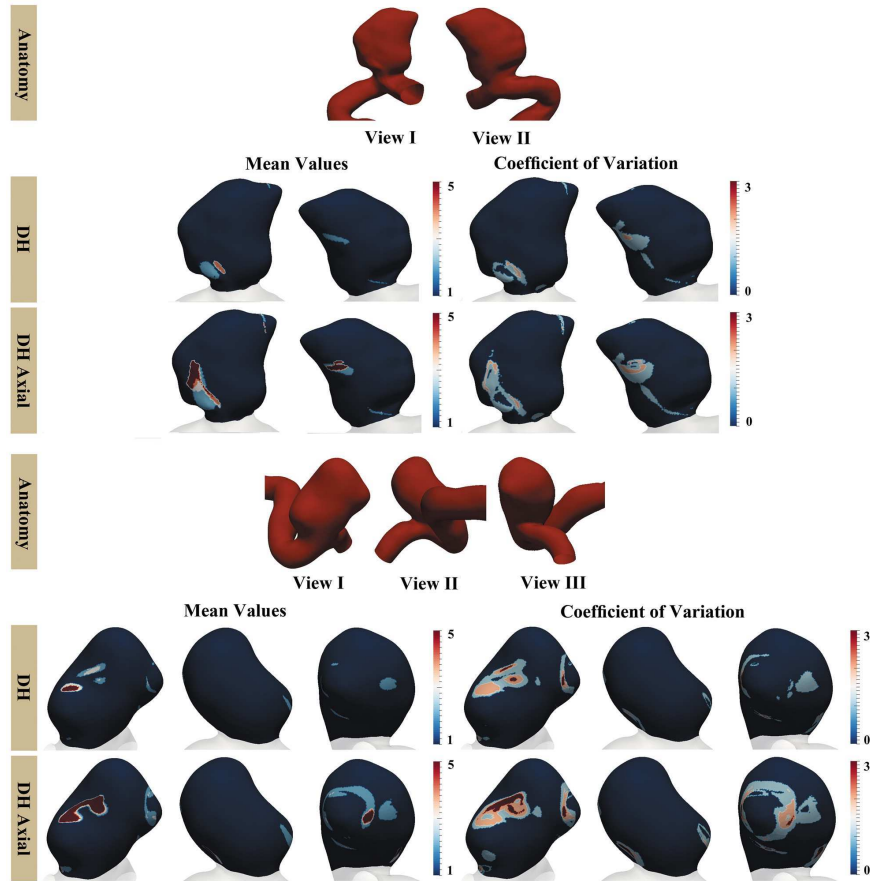


Figure 3: The mean values and the coefficients of variation (CoV) of the dominant harmonic (DH) and axial DH across the virtual population over the aneurysm walls for patients 1 and 2.

274 mostly unidirectional throughout the cardiac cycle (stable flow regions).

275 Fig. 3 shows mean values and CoVs for the dominant harmonic (DH) over
 276 the aneurysm sac. On both aneurysms, there are regions where the dominant
 277 frequencies are up to 5 times greater than the fundamental frequency (the heart
 278 rate). Results show that ICA waveform variability highly influences the time-
 279 varying WSS signal at regions where the higher harmonics dominate (CoV >
 280 2). Similar to the directionality, less significant effects were observed at regions
 281 with regular pulsatile flow dominated by the heart rate frequency (regions where

282 DH is unity).

283 However, DH was originally defined for a unidirectional axial flow and may
284 not lead to clinically interpretable results in multidirectional nonaxial flows (Lee
285 et al. (2009); Morbiducci et al. (2015)). To alleviate this issue in the complex
286 aneurysmal flows, we followed the method presented by Lee et al. (2009) and
287 rectified WSS vectors by projecting them on the time-averaged WSS direction as
288 a reference axial direction. Fig. 3 also shows the effect of parent vessel waveform
289 variability on the harmonic content of the axial WSS magnitude signal. Results
290 show that rectification of the WSS signal increased the DH at regions where flow
291 is multidirectional. This can be attributed to the previously mentioned effects
292 of ICA waveform variations on the WSS directionality, which implicitly affected
293 the WSS magnitude signal during the rectification process. It can be seen that
294 ICA waveform variability significantly influences the harmonic content of the
295 axial WSS at disturbed flow regions ($\text{CoV} > 2$). To provide more intuition
296 into the effects of parent vessel flow waveform variability, we illustrated the
297 results for five manually selected representative points on the aneurysm sacs
298 (see Supplementary Material).

299 *Effect of flow uncertainty on rupture pattern*

300 The three WSS-derived quantities were evaluated through CFD simulations
301 in $N = 38$ cases taken from the @neurIST database. Summary statistics of
302 the WSS values evaluated are shown in Table 1 for the case of mean flow. An
303 unpaired two-sided two-sample t -test was used to select the WSS-related features
304 that were significantly different in the ruptured vs. unruptured populations.
305 Spatially averaged OSI was significant or almost significant for all three flow
306 cases ($p \in [0.032, 0.058]$), whereas TAWSS and TransWSS were not significant
307 for any of the three flow cases considered ($p = 0.7$ for TAWSS and $p \in [0.12, 0.15]$
308 for TransWSS). This was in agreement with the analysis of Bisbal et al. (2011)
309 (who used a superset of our data), but contradicted the observations of Xiang
310 et al. (2014a) who obtained significance also for TAWSS. We therefore opted to
311 train the classifier only on one feature, the OSI, leading to the regression model

	Ruptured ($N = 14$)	Unruptured ($N = 24$)	p -value
TAWSS [Pa]	3.32 (3.36)	3.76 (3.25)	0.7
OSI	12.4×10^{-3} (7.25×10^{-3})	7.79×10^{-3} (6.05×10^{-3})	0.032*
rTransWSS	0.104 (0.037)	0.088 (0.029)	0.12

Table 1: WSS quantities derived from CFD-simulations in the ruptured vs. unruptured groups of the @neurIST cohort. Values are group-wise means and standard deviations of the mean flow case. Statistical significance in univariate analysis computed using a two-sided t -test.

312 $\text{logit}(P_r) = \beta_0 + \beta_1 \text{OSI}$ for the rupture classification variable P_r . Before training
313 the classifier, the OSI values were scaled so that the maximum value across the
314 38 cases was equal to 10. The data were divided into 19 training cases, which
315 were used to estimate the regression coefficients, and 19 test cases, which were
316 used for cross-validation.

317 The logistic regression based classifier achieved an area under the ROC curve
318 that ranged in $\text{AUC} \in [0.8947, 0.9044]$. For the cutoff value $P_r = 0.9$, the
319 resulting classifier achieved a sensitivity ranging in $\text{SENS} \in [79.0\%, 84.2\%]$, and
320 a specificity ranging in $\text{SPEC} \in [79.0\%, 89.5\%]$ in the cross-validation exercise.
321 The regression coefficients identified in each three flow cases were in the range
322 $\beta_0 \in [-3.59, -2.93]$ and $\beta_1 \in [0.804, 0.883]$. The corresponding odds ratio for
323 OSI was in the range $\text{OR}_{\text{OSI}} \in [2.23, 2.42]$, reproducing the known correlation
324 between elevated OSI and rupture status. While the accuracy of the classifier
325 was only moderately affected by the flow case considered, the final rupture/no-
326 rupture prediction changed as a function of flow for 4 cases out of 19.

327 Discussion

328 Recent evidence links the region-specific inflammatory phenotype of the en-
329 dothelial cells to both directionality and harmonic content of the time-varying
330 WSS vector field (Wang et al., 2013; Peiffer et al., 2013a; Mohamied et al.,
331 2015; Himburg et al., 2007; Feaver et al., 2013). Spatiotemporal variations of
332 vascular WSS are driven by variabilities in the blood flow waveform and the vas-
333 cular morphology. Although attempts at measuring the effect of parent vessel

334 flow waveforms on WSS-related quantities of interest measuring directionality
335 and harmonic content have been made by Peiffer et al. (2013a); Himburg et al.
336 (2007); Feaver et al. (2013); Lee et al. (2009) and others, there are few studies
337 that have systematically evaluated the sensitivity of WSS to flow variability.

338 Time-averaged inflow rates have been shown to affect the magnitude of
339 aneurysmal WSS (Geers et al., 2014). Using one-shot measurements of patient-
340 specific inflow boundary conditions has been shown to highly influence the mag-
341 nitude of aneurysmal WSS when compared to results obtained from simulations
342 with typical inflow boundary conditions derived from literature (Karmonik et al.,
343 2010; Marzo et al., 2011; McGah et al., 2014). However, *in vivo* flow measure-
344 ments typically record systemic flow only for a few cardiac cycles, and therefore
345 do not represent the full range of flow variability. In the recent study of Xiang
346 et al. (2014a), the effect of four different inlet waveforms on the space-averaged
347 OSI was tested using CFD. Different waveforms produced drastically different
348 absolute values of OSI, but similar OSI distributions over the aneurysm sac. A
349 linear relationship was also observed between the spatially averaged OSI values
350 calculated using different inflow waveforms, which suggests that changing the
351 waveform did not consistently change the rupture risk ranking of aneurysms.
352 Absolute values of OSI might, however, not be a robust criteria for clinical deci-
353 sion making unless the flow-related uncertainty is explicitly taken into account.

354 We evaluated flow-induced WSS variability by performing simulations us-
355 ing boundary conditions sampled from a statistical description of inter-subject
356 flow variability. When keeping the time-averaged flow rate fixed, variations in
357 ICA flow waveforms had limited effects on the TAWSS over the aneurysm sac.
358 However, it was found that WSS directionality measures (OSI and rTransWSS)
359 in the disturbed flow regions (atheroprone regions) were very sensitive to flow
360 waveform variability, although the effects were limited in regular flow regions
361 where a preferred direction of flow exists (atheroprotective regions). To shed
362 more light on regional effects of flow waveforms on the aneurysmal WSS, we
363 defined atheroprone regions as regions where WSS is low ($TAWSS < 1$ Pa)
364 and multidirectional ($rTransWSS > 0.3$) and atheroprotective regions as re-

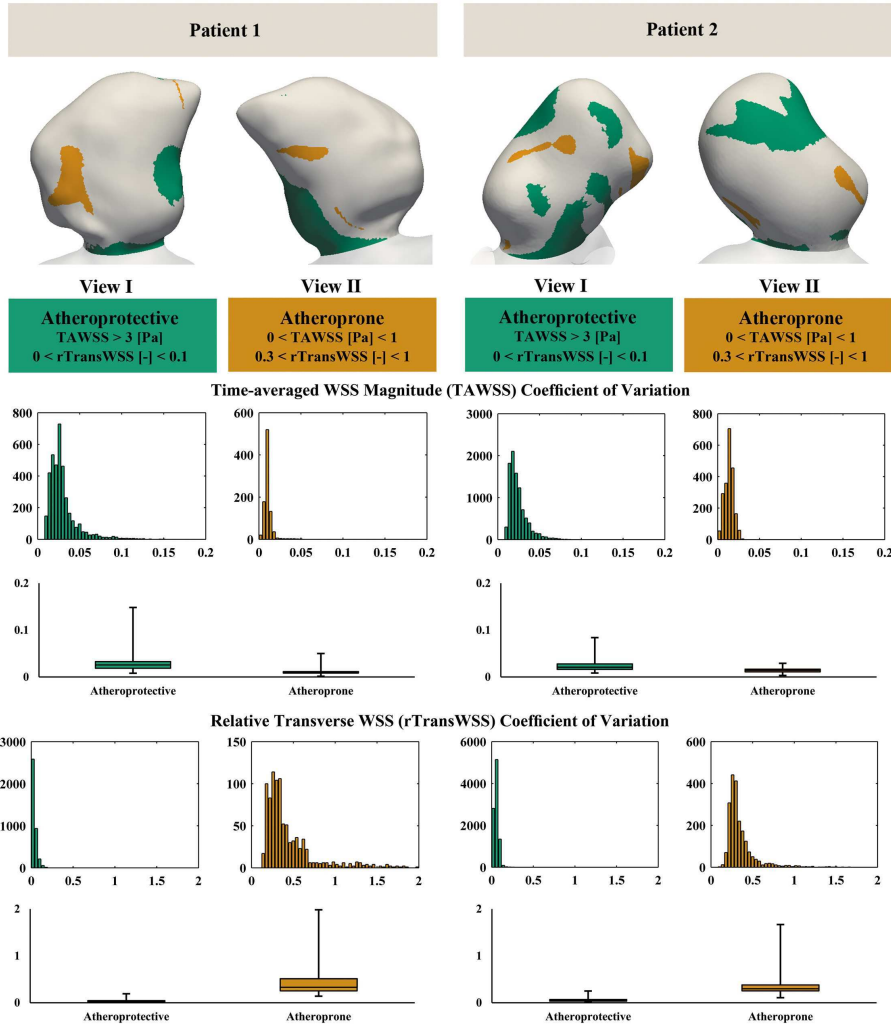


Figure 4: Regional variations of the time-averaged WSS magnitude and the relative transverse WSS. Histograms show the distribution of the coefficient of variations on each of the atheroprone and atheroprotective regions. A boxplot complementary illustration is also presented under each histogram.

365 gions where $TAWSS > 3$ Pa and almost unidirectional ($rTransWSS < 0.1$).
 366 These thresholds were conservatively chosen according to studies where WSS
 367 magnitude and directionality were correlated with pro-inflammatory endothe-

368 lial phenotypes (Wang et al., 2013; Peiffer et al., 2013a; Mohamied et al., 2015;
369 Feaver et al., 2013). As shown in Fig. 4 for the two IAs considered, varying
370 inflow waveform had limited effects on the TAWSS in both disturbed flow and
371 regular flow regions (CoV < 0.1). However, WSS directionality in disturbed
372 flow regions is strongly affected by the inflow waveform (CoV up to 2 with a
373 median at 0.25), when compared to the protective regions. This implies the im-
374 portance of flow waveform uncertainty in aneurysmal regions which are prone
375 to inflammatory phenotypes and potential rupture. Mohamied et al. (2015)
376 observed that despite OSI, TransWSS correlated significantly with atheroscle-
377 rotic lesions in rabbits' aorta. Comparing OSI and rTransWSS as measures of
378 WSS directionality, we observed that these two variables are in stronger cor-
379 relation at regular flow (atheroprotective) regions (Pearson $r = 0.94$ and 0.96
380 for aneurysms 1 and 2, respectively; $p < 10^{-5}$) when compared to disturbed
381 flow (atheroprone) regions where flow is highly multidirectional (Pearson $r =$
382 0.75 and 0.66 for aneurysms 1 and 2, respectively; $p < 10^{-5}$). A point-wise
383 comparison of OSI and rTransWSS is presented in the Supplementary Material.

384 We have studied variability of the DH of the local WSS signal and observed
385 that, due to nonlinear effects due of the vascular morphology, there are regions
386 where the dominant harmonic of the time-varying WSS signal is not the systemic
387 fundamental frequency (heart rate). We observed that, when considering the DH
388 of the axial WSS signals, regions with higher DH than the heart rate co-localise
389 with the regions where flow is multidirectional. This co-localisation could be
390 explained by the fact that axial WSS is the projection of the instantaneous
391 WSS vector in the time-averaged WSS vector direction. Xiang et al. (2014a)
392 observed a strong correlation between the space-averaged aneurysmal OSI and
393 the inflow waveform pulsatility index (PI), and suggested that OSI might be
394 mainly determined by the PI of the inlet waveform. As a subsidiary study, we
395 investigated any possible correlation between the inflow PI and the local OSI at
396 five points on the aneurysm sacs. At each point on the aneurysm sac, PI was
397 calculated as the difference between maximum and minimum flow rate divided
398 by the time-averaged flow rate during each cardiac cycle. No clear correlation

399 was observed between inflow PI and OSI at points where the dominant frequency
400 was higher than the heart rate (see Table 1 in the Supplementary Material).
401 This implies that parent vessel PI (easy to measure) is not a good surrogate for
402 evaluating aneurysmal OSI (difficult to measure).

403 We have also explored the effects that WSS uncertainty may have on IA rup-
404 ture likelihood by using a logistic regression. In our dataset the TAWSS did not
405 reach statistical significance in separating ruptured cases from non-ruptured
406 cases, so that a classifier was built solely based on OSI values. Our classi-
407 fier reached similar accuracy to that previously reported (sensitivity ranging in
408 $\text{SENS} \in [79.0\%, 84.2\%]$ and specificity ranging in $\text{SPEC} \in [79.0\%, 89.5\%]$), but
409 provided a range of values depending on the choice of input flow waveform used.
410 While the accuracy of the classifier was similar across waveforms, the classifi-
411 cation between likely to rupture/likely to not rupture changed in 4 out of the
412 19 cases when the flow solution was varied. It is our view that, due to such ef-
413 fects, flow-related uncertainty should be explicitly accounted for in WSS-based
414 rupture predictions to improve their credibility.

415 The limitations of our study were that the blood flow was assumed to be
416 Newtonian and arterial distensibility was not taken into account, which overes-
417 timates WSS by up to 15% Section (Steinman, 2012). Transition from laminar
418 to turbulent flow occurs at $\text{Re} = 300\text{-}500$ in intracranial aneurysms (Yagi et al.,
419 2013), and using laminar flow models may not capture all intra-aneurysmal flow
420 characteristics accurately. Parabolic velocity profiles were imposed at the in-
421 let boundaries which may lead to different flow characteristics compared to the
422 Womersley profiles. Intra-aneurysmal hemodynamics has been shown to be sen-
423 sitive to the choice of inlet location for truncating the ICA from the surrounding
424 vascular bed (Pereira et al., 2013). To reduce such errors and allow realistic flow
425 inside the aneurysms, all the inlets were truncated at consistent locations below
426 the cavernous segment to include the largest possible arterial segment upstream
427 the aneurysm (Valen-Sendstad et al., 2015). Vascular models were extruded
428 at inlet boundaries by an entry length proportional to the specific Re to allow
429 for fully developed flow. The flow variability model considered also modelled

430 inter-subject variability only (rather than intra-subject), and was based on data
431 from young adults only.

432 **Conflict of interest statement**

433 All the authors declare no conflicts of interest exist.

434 **Acknowledgements**

435 This project was partly supported by the Marie Curie Individual Fellowship
436 (625745, A. Gooya). The aneurysm dataset has been provided by the European
437 integrated project @neurIST (IST-027703).

438 **References**

- 439 Arzani, A., Shadden, S.C., 2016. Characterizations and correlations of wall
440 shear stress in aneurysmal flow. *Journal of Biomechanical Engineering* 138(1),
441 014503.
- 442 Bederson, J.B., Awad, I.A., Wiebers, D.O., Piepgras, D., Haley, E.C., Brott,
443 T., Hademenos, G., Chyatte, D., Rosenwasser, R., Caroselli, C., 2000. Rec-
444 ommendations for the management of patients with unruptured intracranial
445 aneurysms a statement for healthcare professionals from the Stroke Council
446 of the American Heart Association. *Circulation* 102(18), 2300–2308.
- 447 Bisbal, J., Engelbrecht, G., Villa-Uriol, M.C., Frangi, A.F., 2011. Prediction of
448 cerebral aneurysm rupture using hemodynamic, morphologic and clinical fea-
449 tures: a data mining approach, in: A. Hameurlain, S.W. Liddle, K.-D. Schewe,
450 X. Zhou (Eds.), *Database and Expert Systems Applications, Proc. 22nd Int.*
451 *Conf. DEXA 2011, Toulouse, France, August 29–September 2, Springer LNCS*
452 6861. pp. 59–73.
- 453 Bogunović, H., Pozo, J.M., Villa-Uriol, M.C., Majoie, C.B., van den Berg, R.,
454 van Andel, H.A.G., Macho, J.M., Blasco, J., San Román, L., Frangi, A.F.,

455 2011. Automated segmentation of cerebral vasculature with aneurysms in
456 3DRA and TOF-MRA using geodesic active regions: an evaluation study.
457 *Medical Physics* 38(1), 210–222.

458 Bousset, L., Rayz, V., Martin, A., Acevedo-Bolton, G., Lawton, M.T., Higashida, R., Smith, W.S., Young, W.L., Saloner, D., 2009. Phase-contrast
459 magnetic resonance imaging measurements in intracranial aneurysms in vivo
460 of flow patterns, velocity fields, and wall shear stress: comparison with com-
461 putational fluid dynamics. *Magnetic Resonance in Medicine* 61(2), 409–417.

463 Brown, A.G., Shi, Y., Marzo, A., Staicu, C., Valverde, I., Beerbaum, P., Lawford, P.V., Hose, D.R., 2012. Accuracy vs. computational time: translating
464 aortic simulations to the clinic. *Journal of Biomechanics* 45(3), 516–523.

466 Cebal, J.R., Meng, H., 2012. Counterpoint: realizing the clinical utility of
467 computational fluid dynamics—closing the gap. *American Journal of Neuro-
468 radiology* 33, 396–398.

469 Chiu, J.J., Chien, S., 2011. Effects of disturbed flow on vascular endothe-
470 lium: pathophysiological basis and clinical perspectives. *Physiological Re-
471 views* 91(1), 327–387.

472 Davies, P.F., 2009. Hemodynamic shear stress and the endothelium in cardio-
473 vascular pathophysiology. *Nature Reviews Cardiology* 6(1), 16–26.

474 DePaola, N., Gimbrone, M., Davies, P.F., Dewey, C., 1992. Vascular endothe-
475 lium responds to fluid shear stress gradients. *Arteriosclerosis, Thrombosis,
476 and Vascular Biology* 12(11), 1254–1257.

477 Dolan, J.M., Kolega, J., Meng, H., 2013. High wall shear stress and spatial
478 gradients in vascular pathology: a review. *Annals of Biomedical Engineering*
479 41(7), 1411–1427.

480 Feaver, R.E., Gelfand, B.D., Blackman, B.R., 2013. Human haemodynamic
481 frequency harmonics regulate the inflammatory phenotype of vascular en-
482 dothelial cells. *Nature Communications* 4. Article number: 1525.

- 483 Ford, M.D., Alperin, N., Lee, S.H., Holdsworth, D.W., Steinman, D.A., 2005.
484 Characterization of volumetric flow rate waveforms in the normal internal
485 carotid and vertebral arteries. *Physiological Measurements* 26(4), 477.
- 486 Geers, A., Larrabide, I., Morales, H., Frangi, A., 2014. Approximating hemo-
487 dynamics of cerebral aneurysms with steady flow simulations. *Journal of*
488 *Biomechanics* 47(1), 178–185.
- 489 Himburg, H.A., Dowd, S.E., Friedman, M.H., 2007. Frequency-dependent re-
490 sponse of the vascular endothelium to pulsatile shear stress. *American Journal*
491 *of Physiology - Heart and Circulatory Physiology* 293(1), H645–H653.
- 492 Himburg, H.A., Friedman, M.H., 2006. Correspondence of low mean shear and
493 high harmonic content in the porcine iliac arteries. *Journal of Biomechanical*
494 *Engineering* 128(6), 852–856.
- 495 Kallmes, D.F., 2012. Point: CFD—computational fluid dynamics or confound-
496 ing factor dissemination. *American Journal of Neuroradiology* 33, 395–396.
- 497 Karmonik, C., Yen, C., Diaz, O., Klucznik, R., Grossman, R.G., Benndorf,
498 G., 2010. Temporal variations of wall shear stress parameters in intracranial
499 aneurysms—importance of patient-specific inflow waveforms for CFD calcu-
500 lations. *Acta Neurochirurgica* 152, 1391–1398.
- 501 Ku, D.N., Giddens, D.P., Zarins, C.K., Glagov, S., 1985. Pulsatile flow and
502 atherosclerosis in the human carotid bifurcation. positive correlation between
503 plaque location and low oscillating shear stress. *Arteriosclerosis, Thrombosis,*
504 *and Vascular Biology* 5(3), 293–302.
- 505 Lee, S.W., Antiga, L., Steinman, D.A., 2009. Correlations among indicators of
506 disturbed flow at the normal carotid bifurcation. *Journal of Biomechanical*
507 *Engineering* 131(6), 061013.
- 508 Marzo, A., Singh, P., Larrabide, I., Radaelli, A., Coley, S., Gwilliam, M., Wilkin-
509 son, I.D., Lawford, P., Reymond, P., Patel, U., et al., 2011. Computational

510 hemodynamics in cerebral aneurysms: the effects of modeled versus measured
511 boundary conditions. *Annals of Biomedical Engineering* 39, 884–896.

512 McGah, P.M., Levitt, M.R., Barbour, M.C., Morton, R.P., Nerva, J.D., Mourad,
513 P.D., Ghodke, B.V., Hallam, D.K., Sekhar, L.N., Kim, L.J., et al., 2014.
514 Accuracy of computational cerebral aneurysm hemodynamics using patient-
515 specific endovascular measurements. *Annals of Biomedical Engineering* 42,
516 503–514.

517 Meng, H., Tutino, V., Xiang, J., Siddiqui, A., 2014. High WSS or low WSS?
518 complex interactions of hemodynamics with intracranial aneurysm initiation,
519 growth, and rupture: toward a unifying hypothesis. *American Journal of*
520 *Neuroradiology* 35(7), 1254–1262.

521 Mohamied, Y., Rowland, E.M., Bailey, E.L., Sherwin, S.J., Schwartz, M.A.,
522 Weinberg, P.D., 2015. Change of direction in the biomechanics of atheroscle-
523 rosis. *Annals of Biomedical Engineering* 43(1), 16–25.

524 Morales, H.G., Bonnefous, O., 2015. Unraveling the relationship between arte-
525 rial flow and intra-aneurysmal hemodynamics. *Journal of Biomechanics* 48(4),
526 585–591.

527 Morbiducci, U., Gallo, D., Cristofanelli, S., Ponzini, R., Deriu, M.A., Rizzo, G.,
528 Steinman, D.A., 2015. A rational approach to defining principal axes of mul-
529 tidirectional wall shear stress in realistic vascular geometries, with application
530 to the study of the influence of helical flow on wall shear stress directionality
531 in aorta. *Journal of Biomechanics* 48(6), 899–906.

532 Nichols, W., O’Rourke, M., Vlachopoulos, C., 2011. McDonald’s blood flow in
533 arteries: theoretical, experimental and clinical principles. CRC Press.

534 Peiffer, V., Sherwin, S.J., Weinberg, P.D., 2013a. Computation in the rabbit
535 aorta of a new metric—the transverse wall shear stress—to quantify the multi-
536 directional character of disturbed blood flow. *Journal of Biomechanics* 46(15),
537 2651–2658.

- 538 Peiffer, V., Sherwin, S.J., Weinberg, P.D., 2013b. Does low and oscillatory
539 wall shear stress correlate spatially with early atherosclerosis? a systematic
540 review. *Cardiovasc. Res.* DOI: <http://dx.doi.org/10.1093/cvr/cvt044>.
- 541 Pereira, V., Brina, O., Gonzales, A.M., Narata, A., Bijlenga, P., Schaller, K.,
542 Lovblad, K., Ouared, R., 2013. Evaluation of the influence of inlet boundary
543 conditions on computational fluid dynamics for intracranial aneurysms: a
544 virtual experiment. *Journal of biomechanics* 46, 1531–1539.
- 545 Reymond, P., Bohraus, Y., Perren, F., Lazeyras, F., Stergiopulos, N., 2011.
546 Validation of a patient-specific one-dimensional model of the systemic arte-
547 rial tree. *American Journal of Physiology-Heart and Circulatory Physiology*
548 301(3), H1173–H1182.
- 549 Reymond, P., Merenda, F., Perren, F., Rüfenacht, D., Stergiopulos, N., 2009.
550 Validation of a one-dimensional model of the systemic arterial tree. *American*
551 *Journal of Physiology - Heart and Circulatory Physiology* 297(1), H208–H222.
- 552 Steinman, D.A., 2012. Assumptions in modelling of large artery hemodynamics,
553 in: D. Ambrosi, A. Quarteroni, G. Rozza (Eds.), *Modeling of Physiological*
554 *Flows*. Springer-Verlag Italia, pp. 1–18.
- 555 Stergiopulos, N., Young, D., Rogge, T., 1992. Computer simulation of arterial
556 flow with applications to arterial and aortic stenoses. *Journal of Biomechanics*
557 25(12), 1477–1488.
- 558 Valen-Sendstad, K., Piccinelli, M., KrishnankuttyRema, R., Steinman, D.A.,
559 2015. Estimation of inlet flow rates for image-based aneurysm cfd models:
560 where and how to begin? *Annals of biomedical engineering* 43, 1422–1431.
- 561 Valen-Sendstad, K., Steinman, D., 2014. Mind the gap: impact of computational
562 fluid dynamics solution strategy on prediction of intracranial aneurysm hemo-
563 dynamics and rupture status indicators. *American Journal of Neuroradiology*
564 35(5), 536–543.

565 Vignon-Clementel, I.E., Figueroa, C., Jansen, K., Taylor, C., 2010. Outflow
566 boundary conditions for 3d simulations of non-periodic blood flow and pres-
567 sure fields in deformable arteries. *Comput. Methods Biomech. Biomed. Engin.*
568 13(5), 625–640.

569 Villa-Uriol, M., Berti, G., Hose, D., Marzo, A., Chiarini, A., Penrose, J., Pozo,
570 J., Schmidt, J., Singh, P., Lycett, R., et al., 2011. @neurIST complex in-
571 formation processing toolchain for the integrated management of cerebral
572 aneurysms. *Interface Focus* DOI: 10.1098/rsfs.2010.0033.

573 Wang, C., Baker, B.M., Chen, C.S., Schwartz, M.A., 2013. Endothelial cell
574 sensing of flow direction. *Arteriosclerosis, Thrombosis, and Vascular Biology*
575 33(9), 2130–2136.

576 Williams, C.K., Rasmussen, C.E., 2006. Gaussian processes for machine learn-
577 ing. MIT Press 2(3).

578 Xiang, J., Natarajan, S.K., Tremmel, M., Ma, D., Mocco, J., Hopkins, L.N.,
579 Siddiqui, A.H., Levy, E.I., Meng, H., 2011. Hemodynamic–morphologic dis-
580 criminants for intracranial aneurysm rupture. *Stroke* 42(1), 144–152.

581 Xiang, J., Siddiqui, A., Meng, H., 2014a. The effect of inlet waveforms on com-
582 putational hemodynamics of patient-specific intracranial aneurysms. *Journal*
583 *of Biomechanics* 47(16), 3882–3890.

584 Xiang, J., Tutino, V., Snyder, K., Meng, H., 2014b. CFD: computational fluid
585 dynamics or confounding factor dissemination? The role of hemodynamics in
586 intracranial aneurysm rupture risk assessment. *American Journal of Neuro-*
587 *radiology* 35(10), 1849–1857.

588 Yagi, T., Sato, A., Shinke, M., Takahashi, S., Tobe, Y., Takao, H., Murayama,
589 Y., Umezu, M., 2013. Experimental insights into flow impingement in cere-
590 bral aneurysm by stereoscopic particle image velocimetry: transition from a
591 laminar regime. *Journal of The Royal Society Interface* 10, 20121031.